Technical Report

TR-2015-012

Transversally Enriched Pipe Element Method for blood flow modeling

by

L.A. Mansilla Alvarez, P.J. Blanco, C.A. Bulant, E.A. Dari, A. Veneziani, R.A. Feijoo

Mathematics and Computer Science

EMORY UNIVERSITY

Transversally Enriched Pipe Element Method (TEPEM). An effective numerical approach for blood flow modeling

L. A. Mansilla Alvarez[1,2], P. J. Blanco[1,2,*], C. A. Bulant[1,2], E. A. Dari[3], A. Veneziani[4], R. A. Feijóo[1,2]

[1] *National Laboratory for Scientific Computing, LNCC/MCTI, Av. Getúlio Vargas 333, 25651–075, Petrópolis, Brazil*
[2] *National Institute of Science and Technology in Medicine Assisted by Scientific Computing, INCT-MACC, Petrópolis, Brazil*
[3] *CONICET, Centro Atómico Bariloche-CNEA, Instituto Balseiro-UNCUYO, Av. Bustillo 9500, 8400, S.C. de Bariloche, Argentina*
[4] *Department of Mathematics and Computer Science, Emory University, Atlanta (GA), United States*

SUMMARY

In this work we present a novel approach tailored to approximate the Navier-Stokes equations to simulate fluid flow in three-dimensional tubular domains of arbitrary cross-sectional shape. The proposed methodology is aimed at filling the gap between (cheap) one-dimensional and (expensive) three-dimensional models, featuring descriptive capabilities comparable to the full and accurate 3D description of the problem at a low computational cost. In addition, this methodology can easily be tuned or even adapted to address local features demanding more accuracy. The numerical strategy employs finite (pipe-type) elements which take advantage of the pipe structure of the spatial domain under analysis. While low order approximation is used for the longitudinal description of the physical fields, transverse approximation is enriched using high order polynomials. Although our application of interest is computational hemodynamics and its relevance to pathological dynamics like atherosclerosis, the approach is quite general and can be applied in any internal fluid dynamics problem in pipe-like domains. Numerical examples covering academic cases as well as patient-specific coronary arterial geometries demonstrate the potentialities of the developed methodology and its performance when compared against traditional finite element methods.

Received . . .

KEY WORDS: hemodynamics; high order; model order reduction; patient-specific; coronary blood flow

1. INTRODUCTION

The role played by local hemodynamic forces in the initiation and localization of atherosclerosis has been supported by ample evidence gathered from laboratory investigations that include in vivo or in vitro experiments, cell culture studies and gene expression profiling [1, 2, 3, 4, 5, 6, 7, 8, 9, 10]. In this context, image processing tools combined with computational fluid dynamics have made possible the accurate characterization of hemodynamic forces acting over the endothelium.

For the simulation of the cardiovascular system there is a trade-off between computational cost and descriptive capabilities of the models employed. While one-dimensional (1D) models are fundamental to understand global cardiovascular interactions involving wave propagation phenomena [11, 12], three-dimensional (3D) models are mandatory to analyze local blood flow

*Correspondence to: Laboratório Nacional de Computação Científica, Av. Getúlio Vargas 333, Quitandinha, 25651–075, Petrópolis, Brazil, pjblanco@lncc.br

features, such as shear stresses, secondary flows, vorticity, oscillatory shear index (OSI), at specific vascular locations [13, 14, 15, 16].

Concerning coronary blood flow, special interest has been triggered in computational fluid dynamics not only to understand the onset and progress of coronary plaque deposition, but also to be used as a methodology to aid decision-making; for example, these modeling tools are employed to estimate non-invasively the Fractional Flow Reserve (FFR) index [17, 18, 19, 20, 21]. Indeed, expensive 3D models are being employed to accurately characterize the pressure drop across coronary obstructive lesions. In contrast, 1D models present an extremely convenient approach in terms of computational cost, but may definitely have limitations to perform such characterization. Comparisons between 1D and 3D models in the context of blood flow were reported in [22, 23].

In this scenario, there have been increasing efforts in describing blood flow dynamics using reduced data [24], or even improved 1D models [25]. In recent years, the Hierarchical Modeling (HiMod) approach appeared as a promising strategy to deal with models in specific geometries like pipes (and in particular arteries) in a controlled increasing manner.

The basic idea is to split the numerical discretization along the axis of the pipe and the transverse components [26, 27]. The rationale is that we may take computational advantage of the knowledge that the phenomenology of major interest occurs along the axis of the pipe, while the transverse dynamics is important only in some locations. A natural choice to reduce the size of the discrete problem is therefore to discretize the axial dynamics with finite elements - to easily fit centerlines with any shape - and to use spectral methods for the transverse one. In fact, a few degrees of freedom with this method are expected to be enough to capture the dynamics over the transverse sections. This is also justified by the fact that often the transverse sections have a regular shape that can be tackled by spectral approaches. In addition, the number of degrees of freedom can be selected to fit different local accuracies and, for instance, to increase the precision in regions of particular interest (e.g. after a vascular stenosis). Spectral adaptivity may be performed on a piecewise (domain decomposition) setting [28, 27] or even on a nodewise framework [29, 30] coupled with 1D axial grid adaptivity [28] and with time adaptivity [30]. In the context of the Navier-Stokes equations, restricted to straight domains of variable cross sectional diameter, the work by Guzzetti [31] is worth mentioning. Similar ideas were employed to simulate incompressible fluid flow in 2D pipe-like domains in [32]. Results reported in that work were promising towards its aplication to 3D blood flow simulations in curved pipes.

The goal of the present work is to extend the strategy developed in [32] to the case of 3D patient-specific modeling of coronary blood flow. The basic idea of the present methodology is consists in employing pipe-like elements to discretize the domain of analysis. As in HiMod, each pipe element is basically a slab of the tubular domain (the arterial vessel) for which specific axial and cross-sectional interpolation functions are defined. Specifically, physical fields, i.e. fluid velocity and pressure, are approximated using a Cartesian product between polynomial functions of different order, namely low-order for axial coordinate and high-order for transverse coordinates. The combination of the versatility of classical finite element basis functions along the axis combined with an enriched approximation that guarantees accuracy with a few degrees of freedom for the transverse direction significantly reduces the size of the algebraic problem. This strategy is hereafter referred to as *Transversally Enriched Pipe Element Method* (TEPEM). It is important to highlight that arbitrarily shaped cross-sectional areas of the pipes are allowed. We demonstrate here that the TEPEM is able to deliver numerical solutions comparable to standard 3D simulations using the Finite Element Method (FEM), and also we quantify the deviations from such reference solutions when the polynomial order in the transverse direction is diminished. Comparisons against the FEM are presented in terms of solution, problem size and computational time within a parallel implementation paradigm.

Generally speaking, the proposed strategy could be somehow placed in between HiMod techniques and standard general purpose classical finite element techniques. In fact for the transverse dynamics HiMod follows an "educated basis" approach, where the transverse basis functions are constructed to incorporate directly information on the solution like the boundary conditions. This reduces the size of degrees of freedom required and may lead to superconvergence situations as

analyzed in [33] but it is based on the solution of Sturm-Liouville eigenvalue problems that may be non-trivial for non Dirichlet boundary conditions and for general geometries. The approach proposed here relies on a very simple discretization of the domain of analysis into a sequence of slabs, and on the assembly of basis functions on top of those pipe elements (the slabs). Even if the reduction of the degrees of freedom is probably less effective than HiMod for general boundary conditions on the lateral surface of the pipe, for Dirichlet problems it is quite immediate and we demonstrate here that the approach is general, simple and effective for the applications of interest.

The rest of the manuscript is organized as follows. Section 2 presents the setting for the fluid flow problem. Spatial discretization is described in Section 3. Processing of patient-specific geometries is described in Section 4. Academic numerical examples are presented in Section 5, and patient-specific simulations are shown in Section 6. Final remarks are outlined in Section 7.

2. MODEL PROBLEM

Let $\Omega \in \mathbb{R}^3$ with boundary $\Gamma = \Gamma_i \cup \Gamma_o \cup \Gamma_L$, being Γ_i and Γ_o the inlet and outlet (flat) boundaries, respectively. Lateral pipe wall is smooth and is denoted by Γ_L. Figure 1 presents a diagram of the domain of analysis for the fluid flow problem.

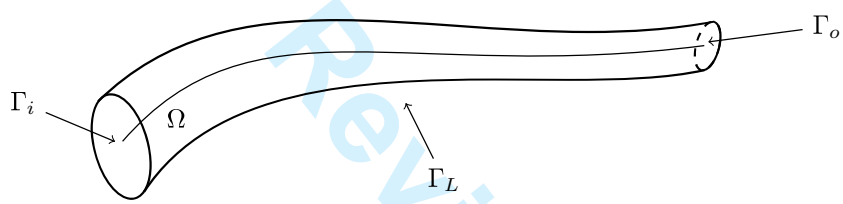

Figure 1. Schematic setting for the model problem.

At Γ_i and Γ_o Neumann or Dirichlet boundary conditions can be imposed. Since we are modeling blood flow in an isolated geometry from the rest of the cardiovascular system, and in order to show the capabilities of our novel approach, we assume that the velocity field is fully developed at Γ_i and Γ_o and uniform Neumann boundary conditions are assumed at those boundaries. Over Γ_L no-slip boundary conditions are considered. These boundary conditions are considered here for simplicity. Other boundary conditions can equally be considered.

The variational formulation for the fluid flow problem reads: find $(\mathbf{u}, p) \in \boldsymbol{\mathcal{V}} \times L^2(\Omega)$ such that

$$\int_\Omega \left[\rho \frac{\partial \mathbf{u}}{\partial t} \cdot \hat{\mathbf{u}} + \rho (\nabla \mathbf{u}) \mathbf{u} \cdot \hat{\mathbf{u}} + 2\mu \boldsymbol{\varepsilon}(\mathbf{u}) \cdot \boldsymbol{\varepsilon}(\hat{\mathbf{u}}) - p \operatorname{div} \hat{\mathbf{u}} - \hat{p} \operatorname{div} \mathbf{u} \right] d\Omega = \int_{\Gamma_i} t_i \mathbf{n} \cdot \hat{\mathbf{u}} \, d\Gamma_i + \int_{\Gamma_o} t_o \mathbf{n} \cdot \hat{\mathbf{u}} \, d\Gamma_o \qquad \forall (\hat{\mathbf{u}}, \hat{p}) \in \boldsymbol{\mathcal{V}} \times L^2(\Omega), \quad (1)$$

with ρ and μ being the fluid density and viscosity, respectively, $\boldsymbol{\varepsilon}(\cdot) = (\nabla(\cdot))^S$ is the symmetric gradient operator, $\mathbf{n}$ is the outward unit vector normal to Γ, t_i and t_o are given data which stand for the magnitude of the normal component of the traction vector imposed at Γ_i and Γ_o, respectively, $\hat{(\cdot)}$ denotes an admissible variation of field $(\cdot)$ and space $\boldsymbol{\mathcal{V}}$ is

$$\boldsymbol{\mathcal{V}} = \{\mathbf{u} \in \mathbf{H}^1(\Omega); \mathbf{u}|_{\Gamma_L} = 0\}, \quad (2)$$

where $\mathbf{H}^1(\Omega) = [H^1(\Omega)]^3$. Here we are referring to the usual notation for functional spaces, i.e. $L^2(\Omega)$ is the Hilbert space of functions whose square is integrable in Ω and $H^1(\Omega)$ is the Sobolev space of functions with values and first derivatives in $L^2(\Omega)$.

We highlight that in the present contribution the development and testing of the numerical methodology is restricted to non-branching domains. The extension to domains featuring

bifurcations can be developed using ideas similar to those published in [32] for 2D problems. For the 3D case this is the matter of ongoing work.

3. TRANSVERSALLY ENRICHED PIPE ELEMENTS

3.1. Geometric mapping

The proposed TEPEM is intrinsecally related to the partition of the domain into slabs. That is, we divide the domain Ω into subdomains $\Omega = \bigcup_{i\in\mathcal{I}} E_i$ where E_i denotes an element of the partition $\mathcal{E}_h$. Each pipe element is a slab of the tubular domain whose axial direction is given by the axial direction of the pipe. A generic element $E \in \mathcal{E}_h$, in the $xyz-$space, is mapped to a reference cubic element E^0 with coordinates (ξ, η, ζ) and with the dominant direction pointing to, say, ζ. Hence, the transverse section of the reference pipe element is in the $\xi\eta$-plane. For the reference element E^0 coordinates are such that $\xi, \eta, \zeta \in [-1, 1]$. The ingredients presented here are shown in Figure 2.

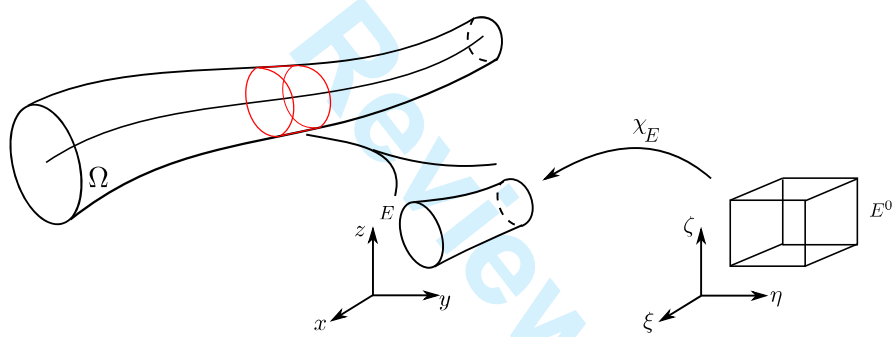

Figure 2. Pipe-elements E are slabs of Ω. Mapping χ_E takes slabs to a cubic reference pipe element E^0.

The mapping χ_E between E and E^0 is defined as follows

$$\chi_E(\xi, \eta, \zeta) = \sum_{k=1}^{3} \chi_k^g(\xi, \eta) Q_k(\zeta), \tag{3}$$

where $\{Q_1, Q_2, Q_3\}$ is a basis for $\mathbb{P}_2$ (quadratic polynomials) in the interval $[-1, 1]$ (i.e. $Q_i = \varphi_i^u$, $i = 1, 2, 3$, see (9) below), and χ_k^g is a mapping between each transverse section $\zeta = k - 2$ at E^0 and the related transverse section at E, $k = 1, 2, 3$. Each one of these transverse mappings is defined as a combination of cubic serendipity polynomials (see Figure 3), that is

$$\chi_k^g(\xi, \eta) = \sum_{i=1}^{12} \mathbf{x}_i^{(k)} \mathcal{S}_i(\xi, \eta) \qquad k = 1, 2, 3 \tag{4}$$

where $\{\mathbf{x}_i^{(k)} = (x_i^{(k)}, y_i^{(k)}, z_i^{(k)}),\ i = 1, \ldots, 12\}$ is the set of points on the transverse section mapped from the section $\zeta = k - 2$ on the reference element, and functions $\mathcal{S}_i$, $i = 1, \ldots, 12$, are

$$
\begin{aligned}
\mathcal{S}_1(\xi,\eta) &= \frac{1}{32}(1+\xi)(1-\eta)(9(\xi^2+\eta^2)-10) & \mathcal{S}_2(\xi,\eta) &= \frac{1}{32}(1+\xi)(1+\eta)(9(\xi^2+\eta^2)-10)\\
\mathcal{S}_3(\xi,\eta) &= \frac{1}{32}(1-\xi)(1+\eta)(9(\xi^2+\eta^2)-10) & \mathcal{S}_4(\xi,\eta) &= \frac{1}{32}(1-\xi)(1-\eta)(9(\xi^2+\eta^2)-10)\\
\mathcal{S}_5(\xi,\eta) &= \frac{9}{32}(1+\xi)(1-\eta^2)(1-3\eta) & \mathcal{S}_6(\xi,\eta) &= \frac{9}{32}(1+\xi)(1-\eta^2)(1+3\eta)\\
\mathcal{S}_7(\xi,\eta) &= \frac{9}{32}(1-\xi^2)(1+3\xi)(1+\eta) & \mathcal{S}_8(\xi,\eta) &= \frac{9}{32}(1-\xi^2)(1-3\xi)(1+\eta)\\
\mathcal{S}_9(\xi,\eta) &= \frac{9}{32}(1-\xi)(1-\eta^2)(1+3\eta) & \mathcal{S}_{10}(\xi,\eta) &= \frac{9}{32}(1-\xi)(1-\eta^2)(1-3\eta)\\
\mathcal{S}_{11}(\xi,\eta) &= \frac{9}{32}(1-\xi^2)(1-3\xi)(1-\eta) & \mathcal{S}_{12}(\xi,\eta) &= \frac{9}{32}(1-\xi^2)(1+3\xi)(1-\eta)
\end{aligned}
\tag{5}
$$

Figure 3 displays the points used in the construction of the proposed cubic serendipity mapping. Hence, mapping (3) results

$$
\chi_E(\xi,\eta,\zeta) = \sum_{k=1}^{3}\sum_{i=1}^{12} \mathbf{x}_i^{(k)} Q_k(\zeta)\mathcal{S}_i(\xi,\eta). \tag{6}
$$

This mapping is affine, and for typical cross-sectional lumen shapes like the ones observed in our numerical tests, we found it to be invertible. A general analysis of the existence inverse map is out of the scope of the present work and will be considered elsewhere.

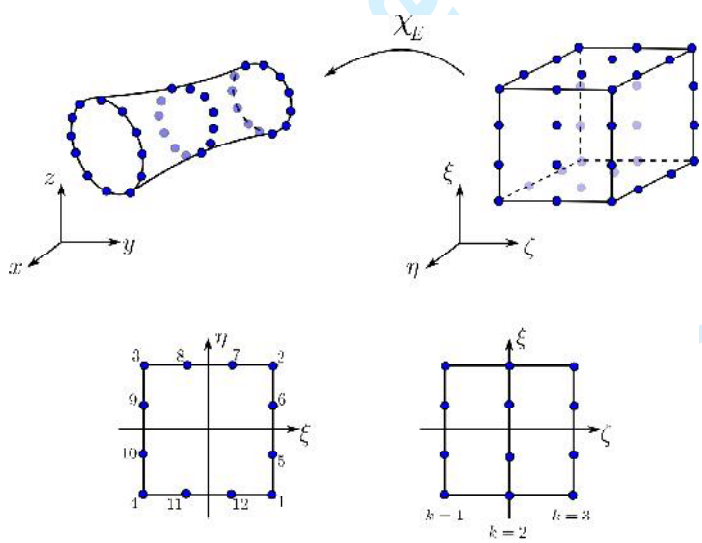

Figure 3. Sub-parametric element and degrees of freedom associated to the geometrical mapping.

3.2. *Basis functions*

The numerical features of the TEPEM reside in the way in which fields are approximated in the reference domain E^0. Let us denote by $\mathbb{P}_G$ the space of polynomials of order $G-1$ and by $\mathbb{P}_G^2 = \mathbb{P}_G \times \mathbb{P}_G$ the cartesian product space. Any scalar field w defined in the original domain Ω is

approximated through the function w^h as follows

$$V_h = \left\{ w^h \in C^0(\overline{\Omega}), w^h(\chi_E(\xi,\eta,\zeta))|_E = \sum_{j=1}^{S}\sum_{i=1}^{G^2} w^{ij}\phi_i(\xi,\eta)\varphi_j(\zeta) \right.$$
$$\left. \forall\, E \in \mathcal{E}_h, \phi_i \in \mathbb{P}^2_G, i = 1,\ldots,G^2, \varphi_j \in \mathbb{P}_S, j = 1,\ldots,S \right\}, \quad (7)$$

For ease of reference, functions ϕ_i are called *transverse polynomials*, and φ_i are *axial polynomials*. Thus, G and S are, respectively, the transverse and axial polynomial orders, and it is considered that $G \gg S$. The real coefficients w^{ij}, $i = 1,\ldots,G^2$, $j = 1,\ldots,S$, define the linear combination.

This approximation strategy allows a natural enrichment of transverse polynomials (simply by increasing the polynomial order) when there is need to simulate complex transverse phenomena. In the context of finite element approximations, the TEPEM is a special choice of interpolants attached to a slab-based meshing strategy. Our main assumption is that the transverse high order approximation allows us to reduce the number of degrees of freedom while being able to accurately predict the physical phenomena.

For the Navier-Stokes problem, each scalar component of velocity field $\mathbf{u} = (u_1, u_2, u_3)$ is approximated as $\mathbf{u}^h = (u_1^h, u_2^h, u_3^h) \in \mathbf{V}_h^u$, where $\mathbf{V}_h^u = [V_h^u]^3 \cap \boldsymbol{\mathcal{V}}$ and $p^h \in V_h^p$, respectively. The space V_h^u is defined as (7) with transverse and axial polynomial orders given by G_u and S_u, respectively. Analogously, for the pressure field p the space is V_h^p, with transverse and axial polynomial orders given by G_p and S_p. Examples of interpolants, for velocity and pressure are detailed below.

Hence, the semi-discrete version of (1) becomes: find $(\mathbf{u}^h, p^h) \in \mathbf{V}_h^u \times V_h^p$ such that

$$\int_\Omega \left[\rho \frac{\partial \mathbf{u}^h}{\partial t} \cdot \hat{\mathbf{u}}^h + \rho(\nabla \mathbf{u}^h)\mathbf{u}^h \cdot \hat{\mathbf{u}}^h + 2\mu\boldsymbol{\varepsilon}(\mathbf{u}^h) \cdot \boldsymbol{\varepsilon}(\hat{\mathbf{u}}^h) - p^h \operatorname{div} \hat{\mathbf{u}}^h - \hat{p}^h \operatorname{div} \mathbf{u}^h \right] d\Omega =$$
$$\int_{\Gamma_i} t_i \mathbf{n} \cdot \hat{\mathbf{u}}^h \, d\Gamma_i + \int_{\Gamma_o} t_o \mathbf{n} \cdot \hat{\mathbf{u}}^h \, d\Gamma_o \qquad \forall (\hat{\mathbf{u}}^h, \hat{p}^h) \in \mathbf{V}_h^u \times V_h^p. \quad (8)$$

The essential boundary conditions over Γ_L are directly imposed by construction in the transverse polynomials $\{\phi_1^u, \ldots, \phi_{G_u^2}^u\}$.

The discrete fully coupled variational equation (8) is further discretized in time by an implicit backward Euler scheme. The convective term is explicitly treated.

An adequate rule to choose polynomial orders to satisfy the inf-sup condition is still a matter of research. However, and inspired in the classical approach of enriching the velocity field with respect to the pressure field, considering $G_u > G_p$ and $S_u > S_p$ leads to stable pairs of velocity-pressure finite-dimensional spaces. In our experience, the rules introduced below are always stable in the sense of the inf-sup condition.

For the axial polynomials, we consider $S_u = 3$ and $S_p = 2$, i.e., a combination of quadratic and linear approximation for the velocity and pressure, respectively, also known as Taylor-Hood finite elements. Then, in the reference element for the dominant direction we have

$$\begin{cases} \varphi_1^u(\zeta) = \frac{1}{2}(\zeta - 1)\zeta \\ \varphi_3^u(\zeta) = \frac{1}{2}(\zeta + 1)\zeta \\ \varphi_2^u(\zeta) = 1 - \zeta^2 \end{cases} \qquad \begin{cases} \varphi_1^p(\zeta) = \frac{1}{2}(1 + \zeta) \\ \varphi_2^p(\zeta) = \frac{1}{2}(1 - \zeta) \end{cases} \quad (9)$$

For the transverse polynomials, the product of two one-dimensional Lagrange polynomials is considered, defined in the coordinates ξ and η. Let G the transverse order, then each $\phi_i \in \mathbb{P}^2_G$ is expressed as

$$\phi_i(\xi,\eta) = \hat{\phi}_j(\xi)\hat{\phi}_k(\eta) \qquad (\xi,\eta) \in [-1,1]^2 \quad (10)$$

where i and (j,k) are related through a bijection between $\{1,\ldots,G^2\}$ and $\{1,\ldots,G\}\times\{1,\ldots,G\}$, and each $\hat{\phi}_j$ has the typical Lagrangian form

$$\hat{\phi}_j(\xi) = \prod_{\substack{m=1\\ m\neq j}}^{G} \frac{(\xi - x_m)}{(x_j - x_m)} \qquad j = 1,\ldots,G. \tag{11}$$

To avoid oscilatory behavior (Runge's phenomenon) of standard Lagrange polynomials set on equidistant points, we choose x_i, $i = 1,\ldots,G$, to be the set of Chebishev–Gauss–Lobatto points.

For the definition of transverse polynomials for velocity and pressure, we consider the following relation between transverse orders

$$G_u = 2G_p - 1. \tag{12}$$

Although other choices are possible, this particular combination is convenient because the nodes for the pressure approximation makes use of a subset of the velocity nodes (nested nodes). Figure 4 shows two sets of nodes corresponding to different transverse orders, where the velocity and pressure degrees of freedom are defined.

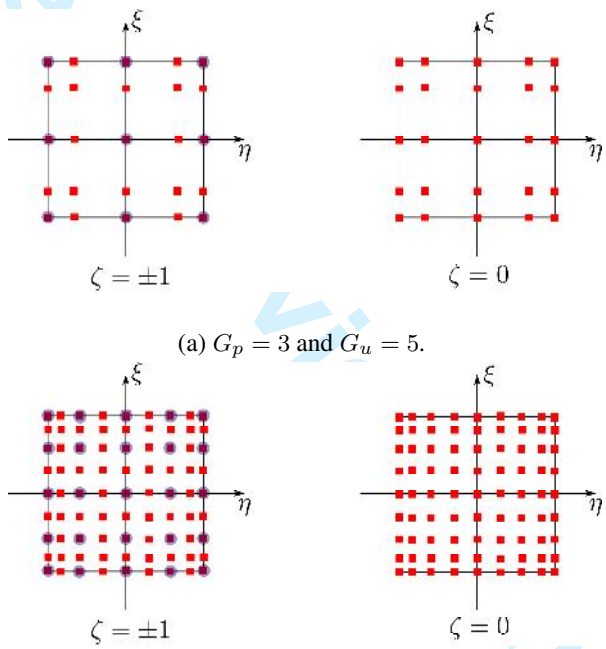

(a) $G_p = 3$ and $G_u = 5$.

(b) $G_p = 5$ and $G_u = 9$.

Figure 4. Velocity (red) and pressure (blue) nodes in each transverse section of a reference element for different transverse order. Transverse nodes are defined on the set of Chebishev–Gauss–Lobatto points. These elements correspond to $S_u = 3$ and $S_p = 2$.

4. GEOMETRIC MODELING

Patient specific arterial domains are constructed combining (i) any processing pipeline to go from image segmentation to finite element surface meshes and (ii) a centerline extraction process plus the identification of curves that define the transverse luminal areas.

Observe that the specificities of step (i) corresponding to the image segmentation pipeline depend on the imaging modality. Step (ii), in turn, does not depend on the modality. For simplicity, in the next section the procedure is explained for the case of Coronary Computed Tomography Angiography (CCTA) images.

4.1. Image segmentation and processing

The image segmentation and mesh processing pipeline used in this work is illustrated in Figure 5, which is specific for to extract arterial structures from CCTA. In this work we focus on non-bifurcating segments of the Left Anterior Descending (LAD) artery. The core image segmentation work-flow is based on two steps: (a) manually selection of two seed points inside the artery, one after the last visible branch and the second in the distal region. The colliding front method [34] is used to obtain an initial segmentation of the artery delimited by the seed points; (b) a level set algorithm [34] initialized with the colliding front output is used to obtain the final segmentation. The level set method produces a gray-scale image whose zero-level represents the arterial lumen. A raw surface triangulation is constructed using the marching cubes method [35], which produces a closed surface.

The mesh processing work-flow consist of four steps: (a) by using techniques and tools described in [36], a centerline is computed from the raw triangulation, and perpendicular clips are performed to open the mesh at the inlet and outlet; (b) such open surface is smoothed and re-meshed to improve quality and achieve quasi-homogeneous triangle size, producing a refined open surface of the arterial lumen. At this point two operations are applied, (c) a tetrahedralization of the refined surface to produce finite element volume meshes to perform standard finite element simulations; (d) a new centerline is computed from the improved surface obtained in (b) and transverse sections are extracted at approximately equidistant centerline points. All these steps make intensive used of the Vascular Modeling ToolKit (VMTK) [37].

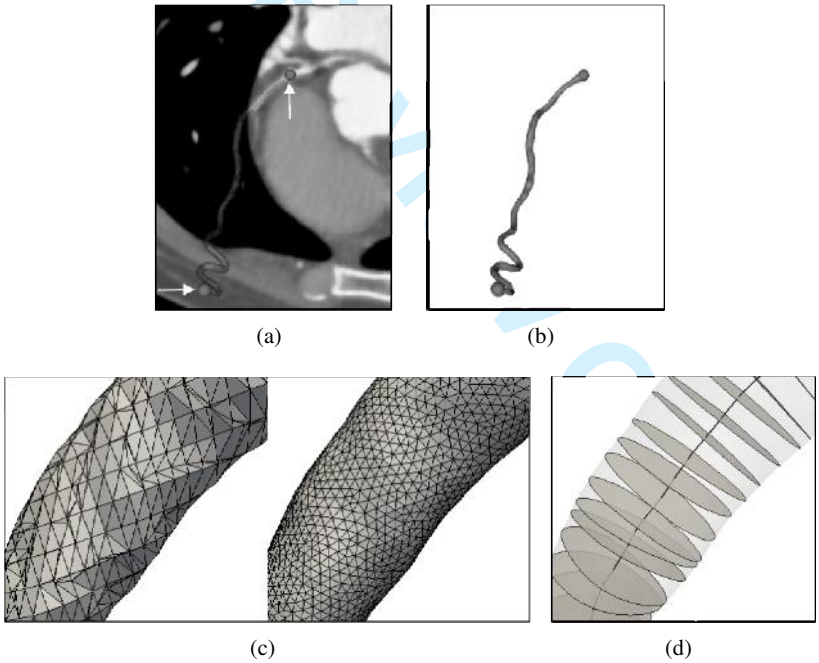

Figure 5. Work-flow of arterial segmentation and geometric modeling stages. Panel (a) shows the input CCTA image with two seed points (arrows) and the colliding front initial segmentation; panel (b) shows the triangulation obtained with marching cubes after level set execution; panel (c) shows a comparison of the raw surface and the improved mesh; panel (d) presents the centerline of the artery with cross sections represented as surfaces.

We point out that the work-flow composed by panels (a) to (c) in Figure 5 is standard for FEM blood flow simulations, and we stress in this case the need for the time-consuming volume meshing stage (c). For the TEPEM proposed in this work we replace stage (c) by stage (d), which amounts for the generation of the centerline and a 1D mesh on top of it consisting of $N_{1\mathrm{D}}$ nodes. At each node i, $i = 1, \ldots, N_{1\mathrm{D}}$, we have the tangent vector to the centerline $\mathbf{s}_i$, which defines the

transversal plane that is used to slice the surface triangulation, generating the polyline $\mathcal{P}_i$. Polylines $\mathcal{P}_i$, $i = 1, \ldots, N_{1\mathrm{D}}$ accurately characterize the cross-sectional geometry of the vessel.

Regardless of the imaging modality, the image segmentation is able to yield a surface triangulation as shown in panel (c) in Figure 5. After that, the procedure is modality-independent. For instance, a raw geometry obtained from Optical Coherence Tomography (OCT) is used in this work to simulate blood flow in a stenotic case. OCT provides a stack of sections of a coronary artery from inside, similar to Intra-Vascular Ultra-Sound (IVUS) but with more resolution. The longitudinal slices can be segmented (some care is needed to complete the lack of information generated by the shadow of the wire) and stacked to be eventually reconstructed in a 3D surface described by a triangulation. This step was performed again with VMTK by a level-set based procedure. Finally, the centerline is generated as explained above. When imaging is based on OCT only, the resulting geometry is quasi-rectilinear, since the centerline coincides with the catheter form a frame of reference moving with it. We selected this case as a first test to focus on local variations of the transverse sections in a rectilinear setting and to demonstrate the applicability of our approach to diverse imaging modalities. It is worth noting that OCT is becoming a popular imaging method in clinical routine of many top medical centers [38]. In more advanced settings (that we will explore in forthcoming works), the 3D reconstruction can be registered with bi-planar angiographies to obtain the truly 3D curved structure (currently obtained only by CCTA as in the second and third cases tested in Section 6) - for more details see [39].

4.2. *Cross-sectional area approximation*

Now, it is necessary to approximate the curves $\mathcal{P}_i$, $i = 1, \ldots, N_{1\mathrm{D}}$ that define the luminal area using the mapping introduced in (4), thus leading to the mapping (6). Such approximation depends upon the choice of points $\mathbf{x}_i$, $i = 1, \ldots, 12$, for each transversal area. We use the least squares method to best approximate the set of polylines $\mathcal{P}_i$ with the set of pipe elements $E = \chi_E(E^0)$.

We assume that the polylines can be satisfactorily approximated by piece-wise polynomial functions which are continuous and with first derivative continuous.

Let $\mathcal{P}(t)$, $0 \le t \le 1$, be a parameterization of the polyline $\mathcal{P}$ and $\mathcal{C}_{\mathbf{x}}(t)$ is a parametrization of the corresponding closed curve $\chi^g(\xi, \eta)$ as given by (4), for $(\xi, \eta) \in [-1, 1]^2$, that is

$$\mathcal{C}_{\mathbf{x}}(t) = \sum_{i=1}^{12} \mathbf{x}_i \mathcal{S}_i(\xi(t), \eta(t)) \qquad (\xi(t), \eta(t)) = \begin{cases} (8t-1, -1) & 0 \le t < 1/4 \\ (1, 8t-3) & 1/4 \le t < 1/2 \\ (5-8t, 1) & 1/2 \le t < 3/4 \\ (-1, 7-8t) & 3/4 \le t \le 1 \end{cases} \tag{13}$$

For this parameterization we denote $t_0^+ = 0$, $t_0^- = 1$, $t_1 = 1/4$, $t_2 = 1/2$, $t_3 = 3/4$, and also notice that by construction the curve is continuous at t_i, $i = 0, \ldots, 3$. Then, the least squares problem incorporating the restriction over the continuity of the first derivative consists in finding, for a given fixed node of the 1D mesh, the set of points $\{\mathbf{x}_i, i = 1, \ldots, 12\}$ such that it is solution of the following minimization problem

$$(\mathbf{x}_1, \ldots, \mathbf{x}_{12}, \lambda_0, \ldots, \lambda_3) = \arg \max_{\gamma_0, \ldots, \gamma_3 \in \mathbb{R}} \min_{\mathbf{w}_1, \ldots, \mathbf{w}_{12} \in \mathbb{R}^3} \mathcal{L}(\mathbf{w}_1, \ldots, \mathbf{w}_{12}, \gamma_0, \ldots, \gamma_3), \tag{14}$$

where

$$\mathcal{L}(\mathbf{w}_1, \ldots, \mathbf{w}_{12}, \gamma_0, \ldots, \gamma_3) = \int_0^1 |\mathcal{C}_{\mathbf{w}}(t) - \mathcal{P}(t)|^2 \, dt + \sum_{i=0}^{3} \gamma_i |\mathcal{C}'_{\mathbf{w}}(t_i^+) - \mathcal{C}'_{\mathbf{w}}(t_i^-)|^2. \tag{15}$$

This least squares approach allows us to obtain the optimal set of points for the interpolation of each cross-sectional area and, with this, to achieve a closed form of the geometrical mapping defined in (6) for arbitrary sections.

Figure 6 illustrates, at four luminal areas in a patient-specific arterial geometry, the points of the polyline $\mathcal{P}$ (blue dots) and the resulting least squares approximation (red solid line). We observe that for usual arterial vessels the proposed approach produces reasonable and satisfactory approximations of the transversal area.

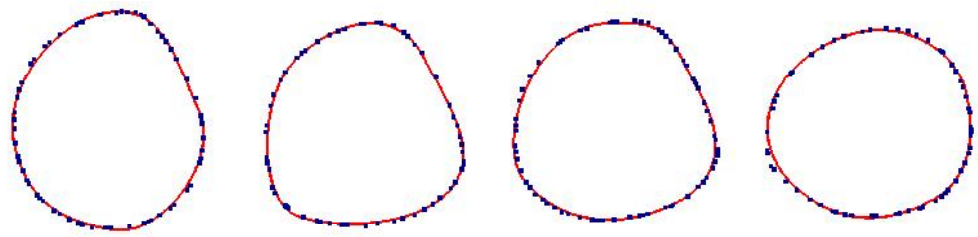

(a) Cross section 1 (b) Cross section 2 (c) Cross section 3 (d) Cross section 4

Figure 6. Approximation of different cross sections via the least squares problem. In each panel we have: blue points of the polyline $\mathcal{P}$ that defines each cross-sectional area, solid red line standing for the approximation.

5. ACADEMIC FLUID FLOW SIMULATIONS

This section presents some examples to test the capabilities of the TEPEM. In this section all quantities are dimensionless.

5.1. *Womersley flow*

Consider the incompressible flow of a fluid inside a cylindrical pipe driven by a pressure gradient oscillating with frequency $\omega = \frac{2\pi}{T}$, where T is the period. The length of the pipe is $l = 2$ and the radius $r = 0.2$. The pressure difference between inlet and outlet is $\Delta p = -A\cos(\frac{2\pi t}{T})$. Amplitude and period are fixed to $A = 2$ and $T = 1$, respectively. Since the velocity profile is fully developed, such pressure difference is imposed using homogeneous (at outlet) and non-homogeneous (at inlet) Neumann boundary conditions, respectively. In addition, homogeneous Dirichlet conditions are applied over the lateral boundaries of the pipe. For the time discretization we consider $\Delta t = \frac{T}{4000}$.

Numerical simulations were performed corresponding to the following Womersley numbers: $\text{Wo} \in \{3, 5, 10, 20\}$. These Wo numbers were reached by varying the fluid viscosity, and keeping the density constant $\rho = 1$. The comparison between the analytical solution and the solution computed with the proposed approach is shown in Figure 7. The approximate solution is taken at the middle of the pipe.

A numerical study of the convergence of the TEPEM was carried out, and is shown in Figure 8 as the transverse approximation order G_u is increased. The convergence is quadratic with G_u. The data reported in Table I shows the error for selected time instants.

It can be seen that even with a low order approximation $G_u = 5$ (see Figure 7), the solution is reasonably good near the wall, which is crucial towards a reasonable, and fast, estimation of the endothelial shear stress in hemodynamic simulations. Also, even for high Wo numbers, the choice $G_u = 9$ offers a very accurate solution. From the convergence study, it is seen that the method features a quadratic convergence with respect to the transverse order.

5.2. *Tortuous pipe*

In this example we consider the steady state flow of a fluid in a tortuous pipe in the xy-plane with circular cross-sectional area. The course of the centerline of the pipe and the radius are, respectively, given by the following formulae

$$y(x) = 0.4\sqrt{x}\sin(\pi x), \tag{16}$$

$$r(x) = 0.1(1 + 0.5\cos^2(\pi x)). \tag{17}$$

For this example we consider 2, 4 and 6 turns of the tortuous pipe, which correspond to 1, 2 and 3 periods in the functions defined above.

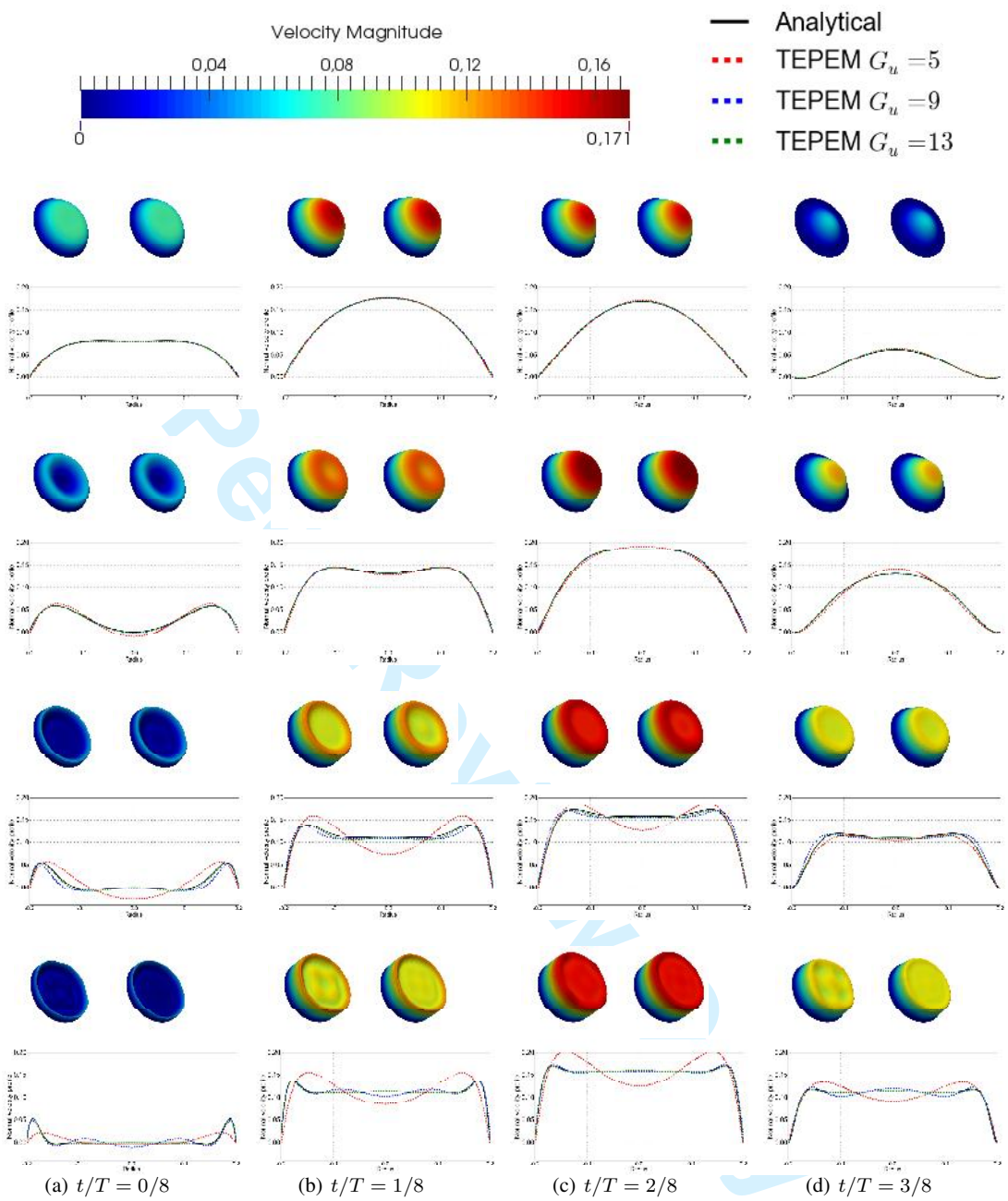

(a) $t/T = 0/8$ (b) $t/T = 1/8$ (c) $t/T = 2/8$ (d) $t/T = 3/8$

Figure 7. Comparison between the TEPEM approximate solution and the analytical solution for different Womersley numbers at for selected time instants. From top to bottom, Wo $\in \{3, 5, 10, 20\}$. Over each plot, the 3D analytical velocity profile (right) and the numerical solution using the TEPEM (left) are shown.

The TEPEM solution is compared to a FEM solution implemented with a standard numerical method [40]. The characteristics of the meshes for both approaches are summarized in Table II. The flow is driven by a pressure difference to reach a given Reynolds number.

The error in the TEPEM solution is computed by comparison against a FEM solution obtained with an extremely fine mesh. The numerical study of the convergence is displayed in Figure 9. The convergence is between quadratic and cubic with respect to G_u.

Table I. Numerical error in the velocity field between the TEPEM solution and the analytical solution measured in the L^2-norm at selected time instants and for different Wo numbers.

		t/T			
		0	1/8	1/4	3/8
Wo = 3	$G_u = 5$	$6.30 \cdot 10^{-4}$	$6.47 \cdot 10^{-4}$	$5.92 \cdot 10^{-4}$	$6.31 \cdot 10^{-4}$
	$G_u = 9$	$1.36 \cdot 10^{-4}$	$1.81 \cdot 10^{-4}$	$1.52 \cdot 10^{-4}$	$1.36 \cdot 10^{-4}$
	$G_u = 13$	$4.62 \cdot 10^{-5}$	$6.53 \cdot 10^{-5}$	$4.31 \cdot 10^{-5}$	$4.62 \cdot 10^{-5}$
Wo = 5	$G_u = 5$	$1.07 \cdot 10^{-3}$	$1.46 \cdot 10^{-3}$	$1.99 \cdot 10^{-3}$	$1.75 \cdot 10^{-3}$
	$G_u = 9$	$3.14 \cdot 10^{-4}$	$5.16 \cdot 10^{-4}$	$4.63 \cdot 10^{-4}$	$2.40 \cdot 10^{-4}$
	$G_u = 13$	$9.81 \cdot 10^{-5}$	$1.81 \cdot 10^{-4}$	$1.42 \cdot 10^{-4}$	$1.08 \cdot 10^{-4}$
Wo = 10	$G_u = 5$	$6.05 \cdot 10^{-3}$	$6.00 \cdot 10^{-3}$	$3.14 \cdot 10^{-3}$	$3.19 \cdot 10^{-3}$
	$G_u = 9$	$2.02 \cdot 10^{-3}$	$1.68 \cdot 10^{-3}$	$1.30 \cdot 10^{-3}$	$1.65 \cdot 10^{-3}$
	$G_u = 13$	$7.56 \cdot 10^{-4}$	$7.97 \cdot 10^{-4}$	$6.77 \cdot 10^{-4}$	$4.46 \cdot 10^{-4}$
Wo = 20	$G_u = 5$	$6.73 \cdot 10^{-3}$	$1.09 \cdot 10^{-2}$	$9.56 \cdot 10^{-3}$	$4.12 \cdot 10^{-3}$
	$G_u = 9$	$2.86 \cdot 10^{-3}$	$2.70 \cdot 10^{-3}$	$3.11 \cdot 10^{-3}$	$2.96 \cdot 10^{-3}$
	$G_u = 13$	$1.15 \cdot 10^{-3}$	$1.28 \cdot 10^{-3}$	$1.11 \cdot 10^{-3}$	$7.56 \cdot 10^{-4}$

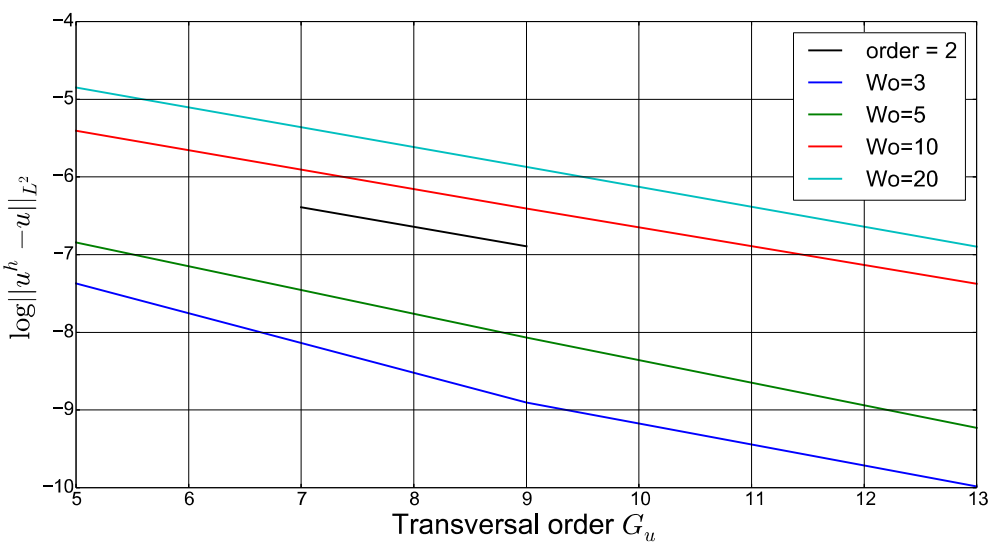

Figure 8. Numerical convergence of the proposed TEPEM approximation methodology for different Womersley numbers.

Table II. Degrees of freedom for the standard FEM approach and for the proposed TEPEM approach in the tortuous pipe problem.

	Degrees of Freedom					Elements	
	FEM	TEPEM				FEM	TEPEM
		$G_u = 7$	$G_u = 9$	$G_u = 11$	$G_u = 13$		
Turn 2	1 329 676	4 407	8 466	13 851	20 562	1 901 141	26
Turn 4	3 054 632	10 383	19 950	32 643	48 462	4 395 739	62
Turn 6	4 139 792	17 355	33 348	54 567	81 012	5 840 736	104

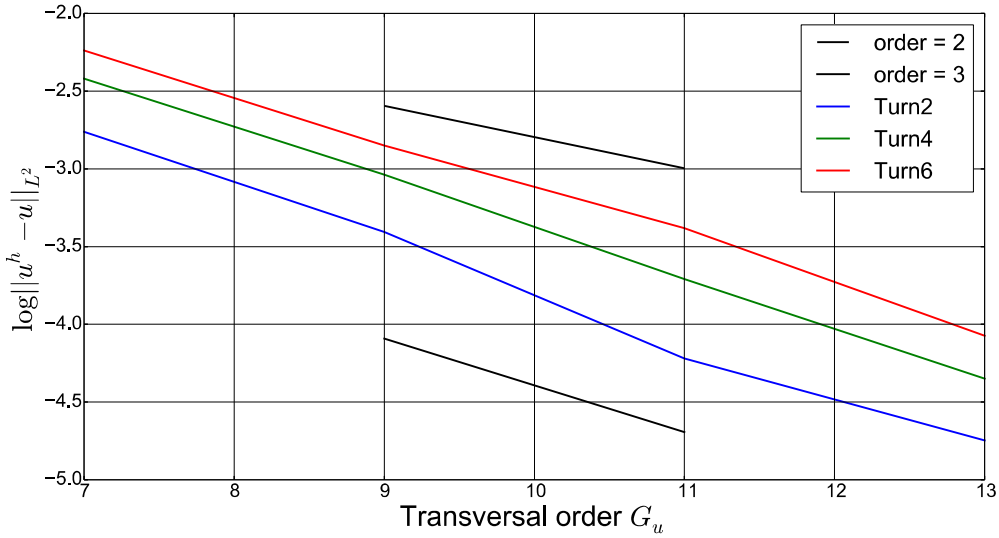

Figure 9. Numerical convergence of the TEPEM by comparison with a reference FEM solution obtained with an extremely fine tetrahedral mesh.

Table III presents the time taken by each method to solve the steady state problem. Although the FEM is considered a reference solution, it can be seen that computing time is reduced from 10 to 900 times. As we increase the size of the problem the TEPEM becomes a more efficient strategy.

Table III. Computational time (in minutes) for the standard FEM approach and for the proposed TEPEM approach for the tortuous pipe problem.

		FEM	TEPEM			
			$G_u = 7$	$G_u = 9$	$G_u = 11$	$G_u = 13$
Re = 50	Turn 2	90	0.5	4	11	25
	Turn 4	390	1	6	22	70
	Turn 6	1 800	3	11	40	125
Re = 500	Turn 2	450	1	10	35	98
	Turn 4	1 900	5	35	95	320
	Turn 6	9 100	10	75	200	660

In order to better understand the improvements in the predictive capabilities of the proposed method, in Figure 10 we present, at several transversal sections, a comparison of the steady state velocity profiles given by the TEPEM, by the reference FEM solution (fine mesh) and by additional FEM solutions obtained with coarse mesh whose characteristic element sizes are of the order of the characteristic distance between the nodes of the TEPEM elements for the corresponding orders G_u (see Figure 4). That is, the coarse FEM mesh for $G_u = 13$ is finer than the coarse FEM mesh for $G_u = 11$, and so on.

From Figure 10, it can be appreciated that, even for $G_u = 7$, the proposed method can satisfactorily solve the normal and transversal components of the velocity vector field for a relatively moderate Reynolds number (Re $= 500$). When we increase G_u we have convergence as expected. In turn, using the corresponding coarse FEM meshes, poor solutions are obtained.

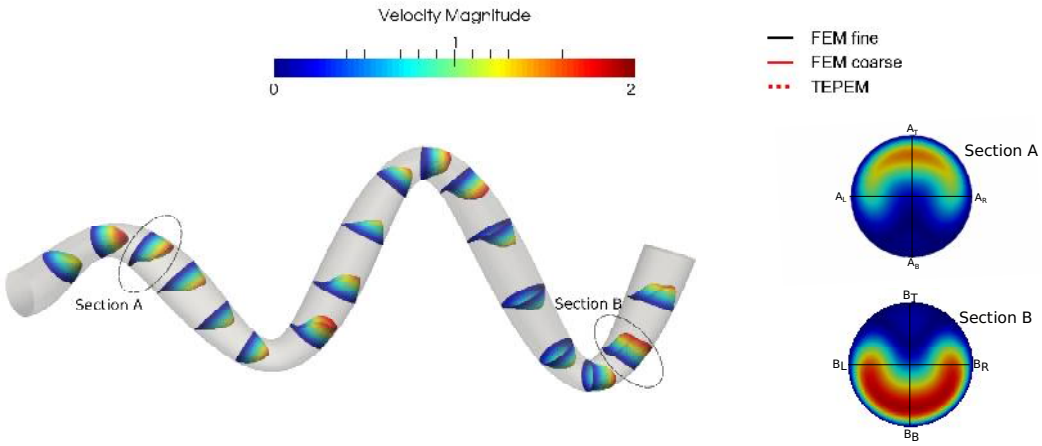

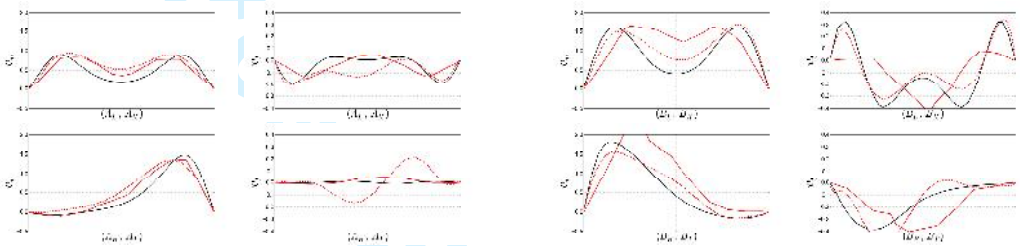

(a) $G_u = 7$. Section A (b) $G_u = 7$. Section B

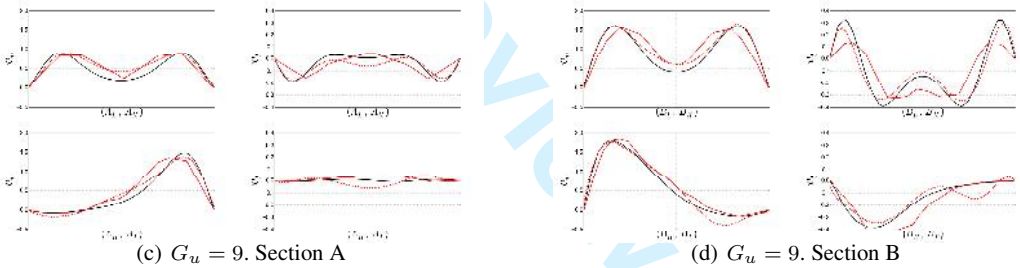

(c) $G_u = 9$. Section A (d) $G_u = 9$. Section B

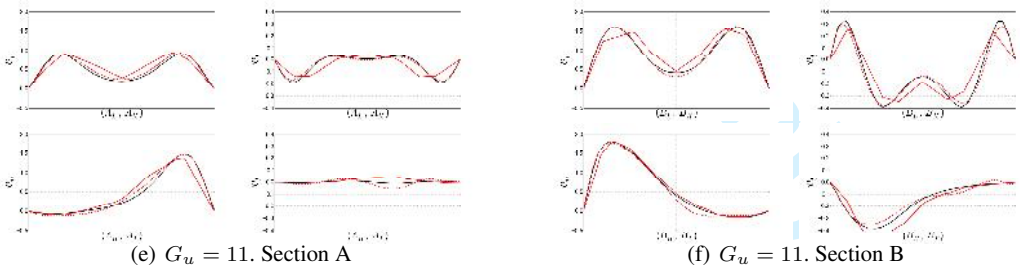

(e) $G_u = 11$. Section A (f) $G_u = 11$. Section B

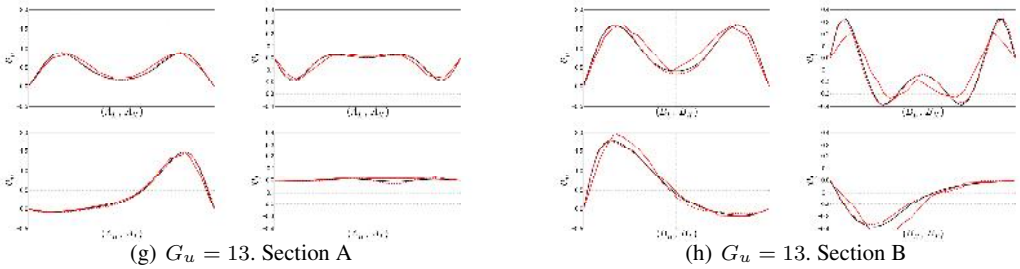

(g) $G_u = 13$. Section A (h) $G_u = 13$. Section B

Figure 10. Comparison of normal and tangential velocity components (v_n and v_t) at selected sections of the tortuous pipe for the case Turn 4 and Re $= 500$. Solutions are compared for different approximation orders of the TEPEM approach and for two (fine and coarse) FEM meshes.

6. CORONARY BLOOD FLOW SIMULATIONS

Patient-specific coronary blood flow simulation is addressed in this section. Three geometries of the left anterior descending (LAD) artery are evaluated: (A) geometry obtained from OCT; (B-C) two geometries obtained from CCTA (see Section 4). These geometric models are shown in Figure 11.

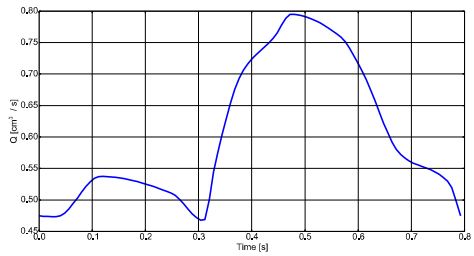

(a) Inflow boundary condition.

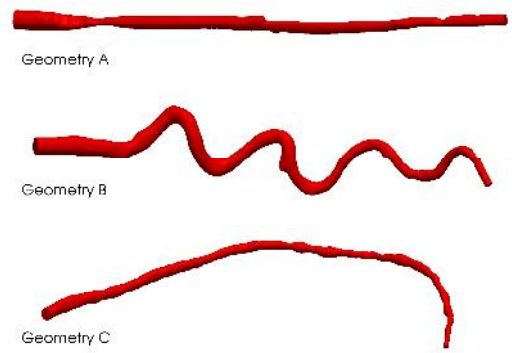

(b) Coronary geometries.

Figure 11. Patient-specific coronary vessels.

The boundary condition at the inlet is given by a prescribed flow rate, which is also shown in Figure 11. This inflow waveform was not measured for the specific patients from whom we collected and reconstructed data. However, we designed this waveform on the basis of available clinical data from Doppler measurements, to guarantee realistic conditions. At the outlet, homogeneous Neumann boundary condition is imposed. Time step is the same for all the cases tests, being $\Delta t = 0.001$ s. Fluid density and viscosity are set to $\rho = 1.04$ g/cm^3 and $\mu = 0.04$ P, respectively. Two cardiac cycles are simulated. A distributed computing paradigm is employed here for both, TEPEM and FEM, because of the size of the problem.

As a first comparison, Figure 12 presents a detail of the blood flow structure for the geometry A at two selected time instants. At the zoomed region, the formation of a vortex is observed. Even for the lower order case ($G_u = 5$), the recirculation region is captured by the TEPEM. And the solution becomes closer to that given by the FEM as we increase the transverse approximation order G_u. It may be worth noting that no 1D model -basically relying on approximating the axial component of the motion- could be able of capturing these vortexes. On the other hand, with TEPEM they are captured with computational costs that are really lower than a full 3D model.

Figures 13, 15 and 17 present the velocity field at several slices in the three coronary geometries considered for two time instants. The solutions obtained using different approximation order for the TEPEM ($G_u \in \{5, 7, 9\}$) are compared with the solution obtained using FEM. The velocity field delivered by the proposed method is very close to the reference one obtained using the FEM. As before, the higher the order of the polynomial approximation for the velocity given by G_u, the better the TEPEM solution.

From the point of view of the potential clinical use of this class of simulations, it is fundamental to analyze the wall shear stress produced by the blood flow over the endothelial wall. The wall shear stress averaged over the cardiac cycle (AWSS) was computed for all the geometries, and the results are presented in Figures 14, 16 and 18. In panels 14(a), 16(a) and 18(a), it can be seen that the spatial distribution of the AWSS obtained with the TEPEM is comparable to that obtained using the FEM. Even the low order approximation given by $G_u = 5$ delivers a reasonably satisfactory solution in terms of AWSS, which can be improved as G_u is increased. Noteworthy, this feature holds for the geometry A which is characterized by the presence of stenoses, for geometry B which is characterized by the highly tortuous geometric pattern, and for geometry C which is characterized by a continuously tapering along with a highly variable vessel radius.

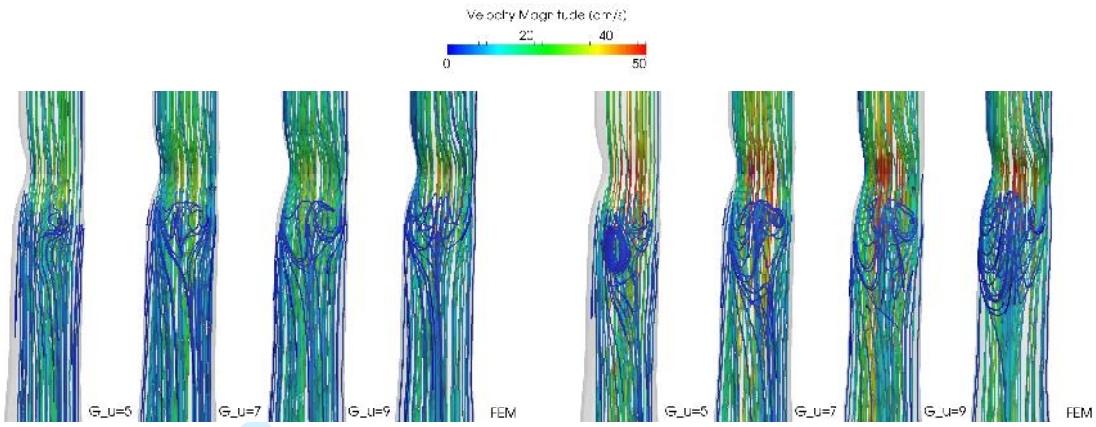

(a) $t = 0.3$ s (b) $t = 0.6$ s

Figure 12. Detail of a recirculation region in the flow structure developed in geometry A as given by different approximation orders of the TEPEM and the FEM at selected time instants.

To further compare the AWSS, the cross sectional average of the AWSS was computed throughout the vessel intrinsic coordinate denoted by s. The results are shown in panels 14(b), 16(b) and 18(b). For geometry A (panel 14(b)) it is seen that three peaks characterize the AWSS which is consistent with the presence of stenoses and bifurations (not considered in the geometry). For geometry B the increase and large variability of the AWSS is caused by the tortuous tapered vessel, and for geometry C a similar pattern but with higher variability is observed. Remarkably, considering the AWSS delivered by the FEM solution as the reference solution, it is observed that the AWSS is excellently well predicted by the TEPEM.

The previous analysis is complemented by a node-wise comparison of the AWSS given by the FEM approximation and the one given by the TEPEM approach using scatter plots as displayed in Figure 19. The theoretical line at $45°$ is shown as well as the correlation coefficient (ρ). It is seen that for all the geometries the correlation is extremely high, and, as expected, it improves as G_u is increased.

The average theoretical time (time multiplied by the number of computing nodes) taken to perform a single time-step in the simulations is presented in Table IV. The number of computing nodes (CN) for the FEM is 160, and for the TEPEM is 36. It is observed that the reduction in the computational time approximately ranges from 10 for $G_u = 9$, to more than 150 or 600 times for $G_u = 5$, depending on the geometry. Recall that the larger the problem the more the reduction in computing time (see Section 5). In view of the capabilities of the present approach to approximate wall shear stress, the proposed method turns to be an excellent choice to speed up hemodynamic simulations.

Method		Time × CN			Mesh DOFs		
		A	B	C	A	B	C
FEM		43.9	69.4	73.1	1 301 868	1 611 428	1 910 760
TEPEM	$G_u = 5$	0.3	0.1	0.1	6 714	5 769	7 659
	$G_u = 7$	2.2	1.2	1.3	17 687	15 197	20 177
	$G_u = 9$	5.4	4.9	5.8	33 986	29 201	38 771

Table IV. Comparison of averaged computational time (in minutes) to perform a single time-step in the FEM and TEPEM implementations. Average time multiplied by the number of computing nodes (CN) used in the simulations is reported. FEM simulations were run with CN $= 160$, while TEPEM simulations were run with CN $= 36$. The number of degrees of freedom (DOFs) in the corresponding meshes is also reported.

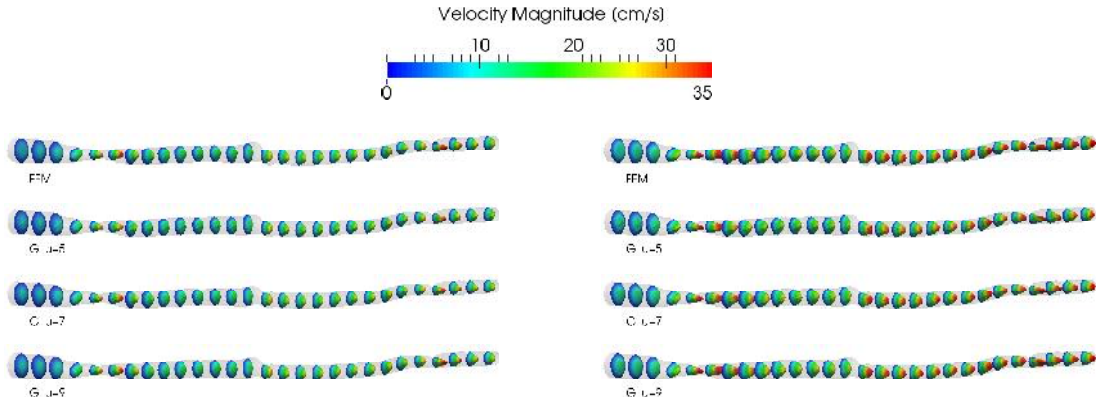

(a) $t = 0.2$ s (b) $t = 0.5$ s

Figure 13. Patient A. Comparison of velocity profiles for different approximation orders of the TEPEM and the FEM at selected time instants.

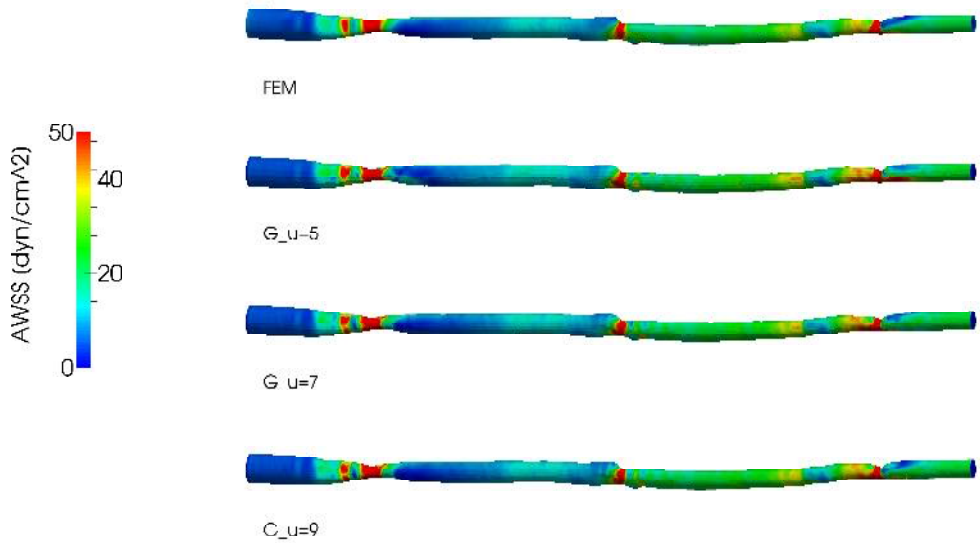

(a) Spatial distribution of AWSS.

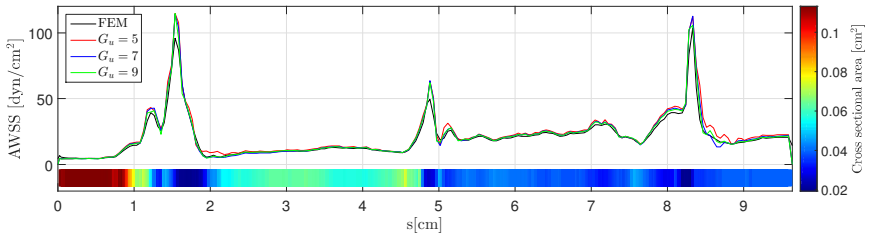

(b) Cross-sectional average of AWSS along the longitudinal coordinate.

Figure 14. Patient A. Comparison of average wall shear stress (AWSS) between FEM and different orders (G_u) of the TEPEM.

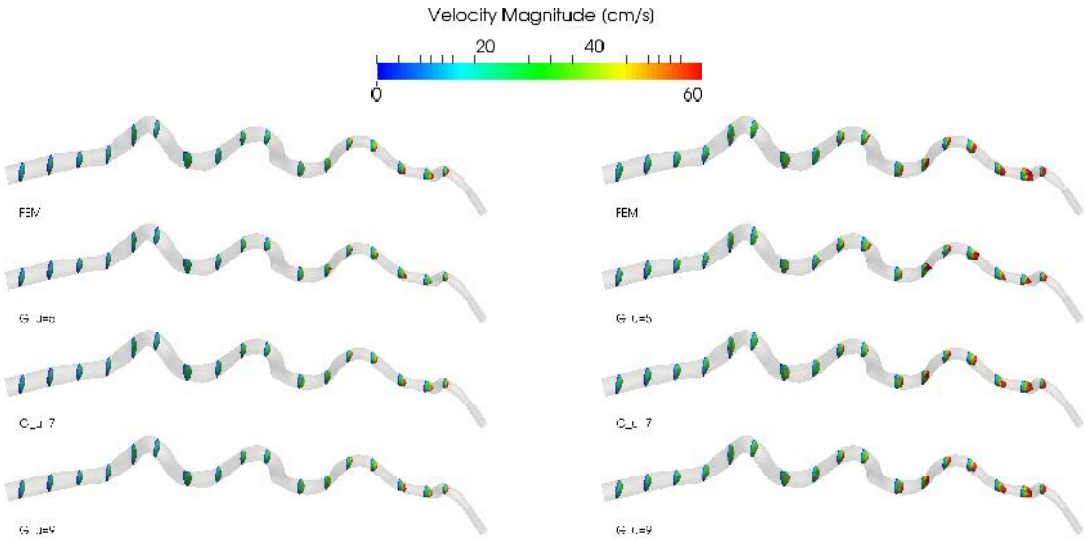

(a) $t = 0.2$ s (b) $t = 0.5$ s

Figure 15. Patient B. Comparison of velocity profiles for different approximation orders of the TEPEM and the FEM at selected time instants.

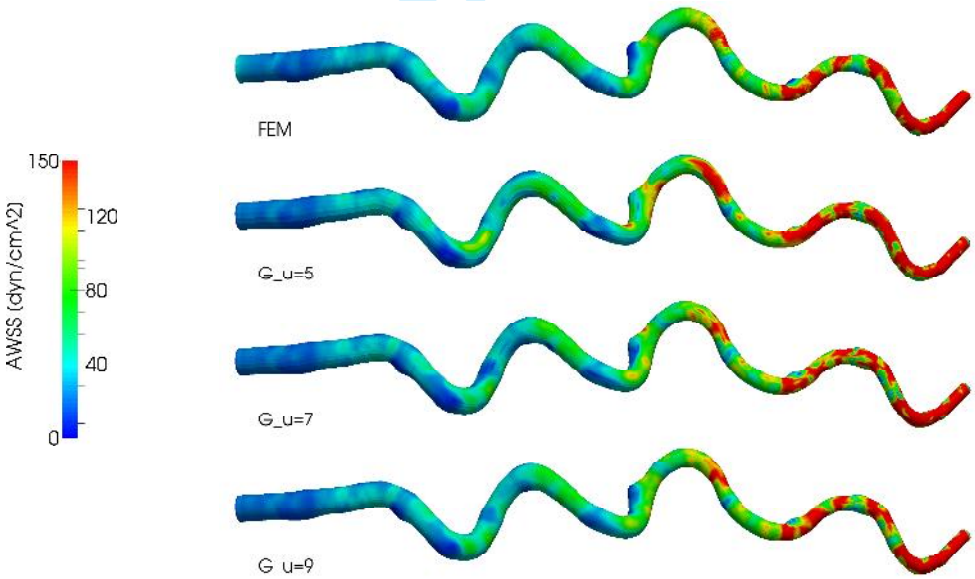

(a) Spatial distribution of AWSS.

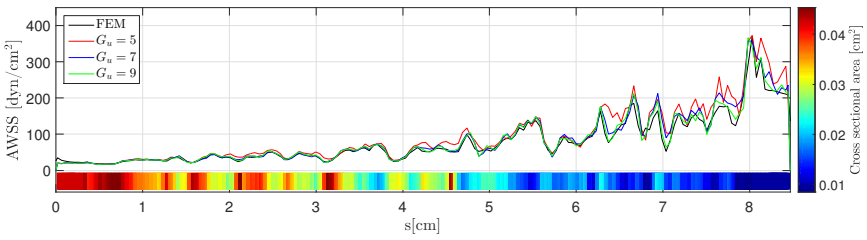

(b) Cross-sectional average of AWSS as a function of the longitudinal coordinate s.

Figure 16. Patient B. Comparison of average wall shear stress (AWSS) between FEM and different orders (G_u) of the TEPEM.

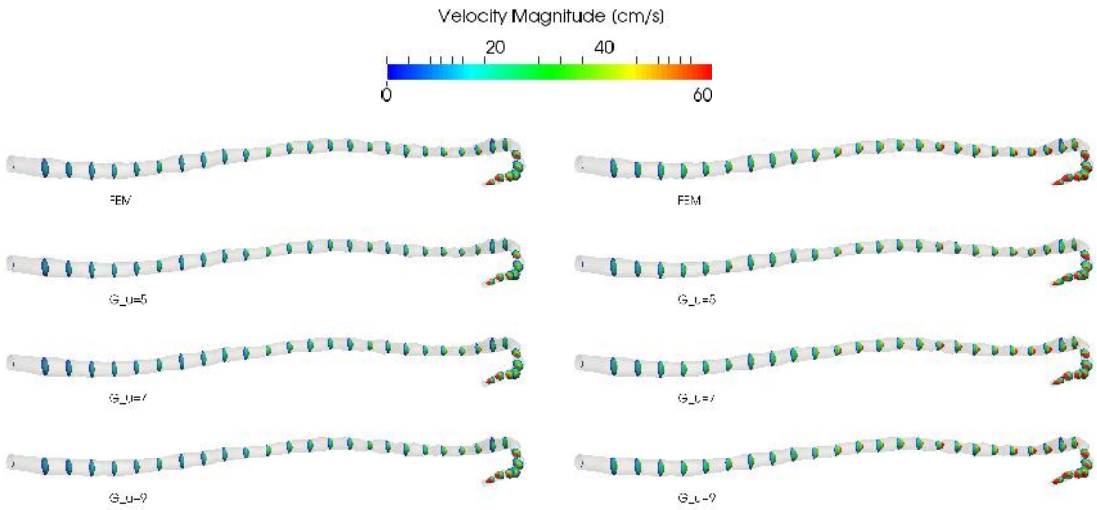

(a) $t = 0.2$ s (b) $t = 0.5$ s

Figure 17. Patient C. Comparison of velocity profiles for different approximation orders of the TEPEM and the FEM at selected time instants.

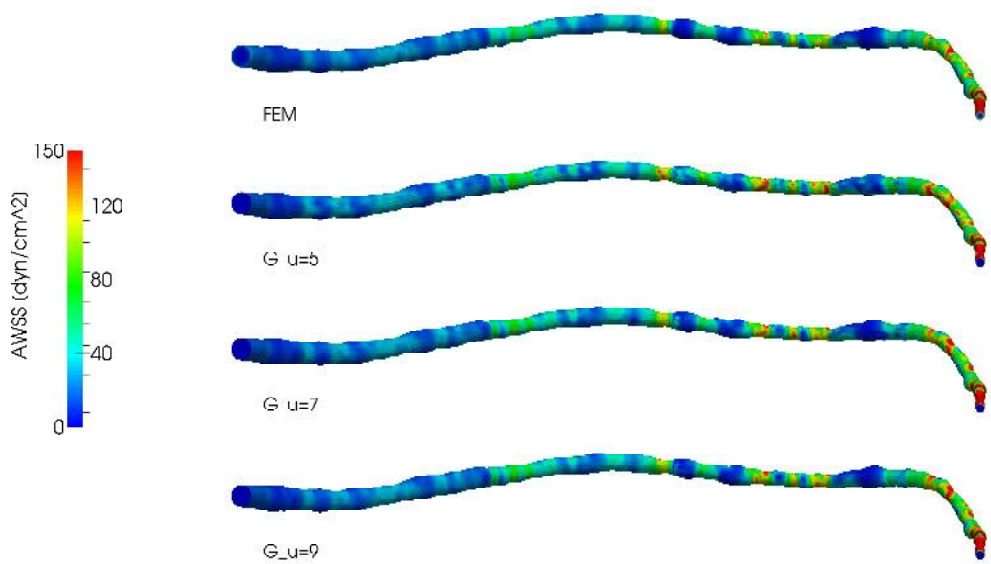

(a) Spatial distribution of AWSS.

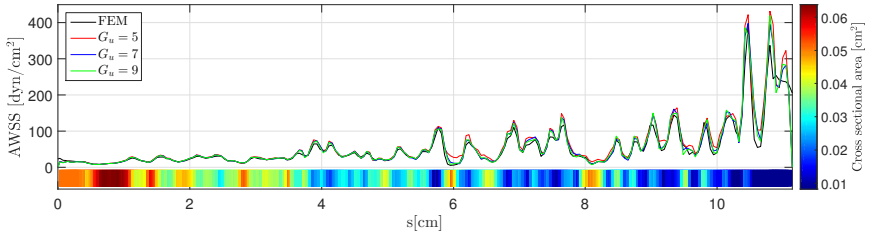

(b) Cross-sectional average of AWSS as a function of the longitudinal coordinate s.

Figure 18. Patient C. Comparison of average wall shear stress (AWSS) between FEM and different orders (G_u) of the TEPEM.

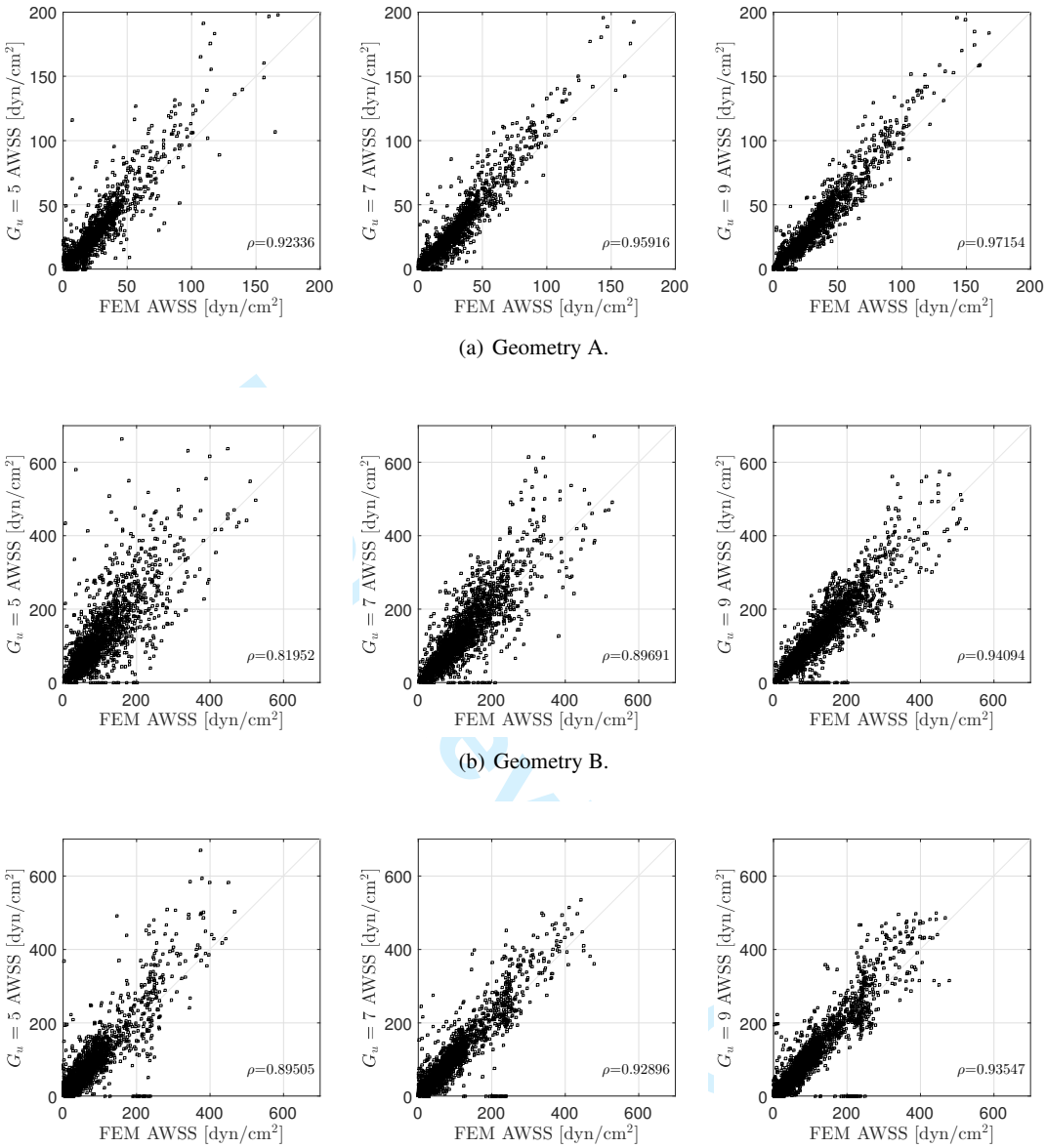

(a) Geometry A.

(b) Geometry B.

(c) Geometry C.

Figure 19. Correlation between AWSS obtained with the TEPEM (for different orders of transversal enrichment) and that obtained using the FEM.

7. FINAL REMARKS

In this work, we have developed a simple strategy for the approximation of the Navier-Stokes equations in pipe-like domains coined Transversally Enriched Pipe Element Method (TEPEM). The basic idea is to combine low order approximation for the physical fields in the longitudinal direction of the pipe with enriched high order approximants for the description in the transverse direction of the pipe. The methodology was exhaustively tested in academic examples against analytic solutions and in patient-specific coronary artery geometries against standard finite element solutions.

The potentialities of the proposed method include large descriptive capabilities regarding the fluid flow physical fields, with emphasis to the wall shear stress, which is of the utmost

importance in cardiovascular research. Furthermore, even for transverse low order approximation (polynomial functions of order four) the wall shear stress was satisfactorily estimated with a gain in computational time ranging between 150 and 600 for the geometries tested.

A further improvement for the treatment of axial dynamics may be the replacement of classical finite elements along the centerline with an IsoGeometric approach, where the solution is described in terms of the same spline-based functions used to represent the non rectlinear axis. This approach -called HIGAMod [41]- will be explored in a follow up of the present work.

ACKNOWLEDGEMENT

This work was partially supported by the Brazilian agencies CNPq and FAPERJ. The support of these agencies is gratefully acknowledged. We also wish to acknowledge the support of the US National Science Foundation - Project DMS 1419060 “Hierarchical Model Reduction Techniques for Incompressible Fluid Dynamics and Fluid-Structure Interaction Problems” (2014-2017). In addition, we thank Dr. G. Guagliumi (Cardiovascular Department. A.O. Papa Giovanni XXIII Hospital, Bergamo, Italy) for providing the OCT data and Dr. M. Piccinelli (Department of Radiology, Emory University, Atlanta (GA) USA) for performing the 3D reconstruction of the geometry of the first coronary artery (Patient A) in Section 6.

REFERENCES

1. Nerem R, Cornhill J. The role of fluid mechanics in atherogenesis. *J. Biomech. Engrg.* 1980; **102**:181–189.
2. Friedman M, Deters O, Mark F, Bargeron C, Hutchins G. Arterial geometry affects hemodynamics. A potential risk factor for athersoclerosis. *Atherosclerosis* 1983; **46**:225–231.
3. Zarins C, Giddens D, Bharadvaj B, Sottiurai V, Mabon R, Glagov S. Carotid bifurcation atherosclerosis. Quantitative correlation of plaque localization with flow velocity profiles and wall shear stress. *Circ. Res.* 1983; **53**:502–514.
4. Ku D, Giddens D, Zarins C, Glagov S. Pulsatile flow and atherosclerosis in the human carotid bifurcation. Positive correlation between plaque location and low oscillating shear stress. *Arteriosclerosis* 1985; **5**:293–302.
5. Friedman M, Deters O, Bargeron C, Hutchins G, Mark F. Shear-dependent thickening of the human arterial intima. *Atherosclerosis* 1986; **60**:161–171.
6. Giddens D, Zarins C, Glagov S. The role of fluid mechanics in the localization and detection of atherosclerosis. *J. Biomech. Engrg.* 1993; **115**:588–594.
7. Chen BP, Li YS, Zhao Y, Chen KD, Li S, Lao J, Yuan S, Shyy JY, Chien S. DNA microarray analysis of gene expression in endothelial cells in response to 24-h shear stress. *Physiological Genomics* Oct 2001; **7**(1):55–63.
8. Davies PF, Polacek DC, Shi C, Helmke BP. The convergence of haemodynamics, genomics, and endothelial structure in studies of the focal origin of atherosclerosis. *Biorheology* 2002; **39**(3):299–306.
9. Gibson CM, Daz L, Kandarpa K, Sacks FM, Pasternak RC, Sandor T, Feldman C, Stone PH. Relation of vessel wall shear stress to atherosclerosis progression in human coronary arteries. *Arteriosclerosis, Thrombosis, and Vascular Biology* 1993; **13**(2):310–315.
10. Molony D, Timmins L, Hung O, Rasoul-Arzrumly E, Samady H, Giddens D. An assessment of intra-patient variability on observed relationships between wall shear stress and plaque progression in coronary arteries. *BioMedical Engineering OnLine* 2015; **14(Suppl 1)**:S2.
11. Blanco P, Watanabe S, Dari E, Passos M, Feijóo R. Blood flow distribution in an anatomically detailed arterial network model: criteria and algorithm. *Biomechanics and Modeling in Mechanobiology* 2014; **13**:1303–1330.
12. Blanco P, Watanabe S, Passos M, Lemos P, Feijóo R. An anatomically detailed arterial network model for one-dimensional computational hemodynamics. *IEEE Transactions on Biomedical Engineering* 2015; **62**:736–753.
13. Taylor C, Hughes T, Zarins C. Finite element modeling of blood flow in arteries. *Comp. Meth. Appl. Mech. Engrg.* 1998; **158**:155–196.
14. Cebral J, Yim P, Lohner R, Soto O, Choyke P. Blood flow modeling in carotid arteries with computational fluid dynamics and MR Imaging. *Acad. Radiol.* 2002; **9**:1286–1299.
15. Cebral J, Castro M, Appanaboyina S, Putman C, Millan D, Frangi A. Efficient pipeline for image-based patient-specific analysis of cerebral aneurysm hemodynamics: technique and sensitivity. *IEEE Trans. Med. Imaging* 2005; **24**:457–467.
16. Coskun A, Chen C, Stone P, Feldman C. Computational fluid dynamics tools can be used to predict the progression of coronary artery disease. *Physica A* 2006; **362**:182–190.
17. Grunau G, Min J, Leipsic J. Modeling of fractional flow reserve based on coronary CT angiography. *Curr. Cardiol. Rep.* 2013; **15**:336.
18. Zarins C, Taylor C, Min J. Computed fractional flow reserve ($\mathrm{FFT_{CT}}$) derived from coronary CT angiography. *J. of Cardiovasc. Trans. Res.* 2013; **6**:708–714.
19. Morris P, Ryan D, Morton A, Lycett R, Lawford P, Hose D, Gunn J. Virtual fractional flow reserve from coronary angiography: modeling the significance of coronary lesions: results from the VIRTU-1 (VIRTUal Fractional Flow Reserve From Coronary Angiography) study. *JACC Cardiovascular Interventions* 2013; **6**:149–157.

20. Morris P, van de Vosse F, Lawford P, Hose D, Gunn J. "Virtual" (computed) fractional flow reserve: current challenges and limitations. *JACC Cardiovascular Interventions* 2015; **8**:1009–1017.
21. Tu S, Barbato E, Köszegi Z, Yang J, Sun Z, Holm N, Tar B, Li Y, Rusinaru D, Wijns W, *et al.*. Fractional flow reserve calculation from 3-dimensional quantitative coronary angiography and TIMI frame count: a fast computer model to quantify the functional significance of moderately obstructed coronary arteries. *JACC: Cardiovascular Interventions* 2014; **7**:768–777.
22. Grinberg L, Cheever E, Anor T, Madsen J, Karniadakis G. Modeling blood flow circulation in intracranial arterial networks: A comparative 3D/1D simulation study. *Ann. Biomed. Engng.* 2011; **39**:297–309.
23. Reymond P, Crosetto P, Deparis S, Quarteroni A, Stergiopulos N. Physiological simulation of blood flow in the aorta: comparison of hemodynamic indices as predicted by 3-D FSI, 3-D rigid wall and 1-D models. *Medical Engineering and Physics* 2013; **35**:784–791.
24. Alastruey J, Siggers J, Peiffer V, Doorly D, Sherwin S. Reducing the data: Analysis of the role of vascular geometry on blood flow patterns in curved vessels. *Phys. Fluids* 2012; **24**:031 902.
25. Carapau F, Sequeira A. 1D models for blood flow in small vessels using the Cosserat theory. *WSEAS Transactions on Mathematics* 2006; **5**:54–62.
26. Perotto S, Ern A, Veneziani A. Hierarchical local model reduction for elliptic problems: A domain decomposition approach. *Multiscale Modeling & Simulation* 2010; **2**:1102–1127.
27. Ern A, Perotto S, Veneziani A. Hierarchical model reduction for advection-diffusion-reaction problems. *Numerical Mathematics and Advanced Applications, K. Kunisch, G. Of and O. Steinbach eds.*, Springer, 2008; 703–710.
28. Perotto S, Zilio A. Hierarchical model reduction: three different approaches. *Numerical Mathematics and Advanced Applications, A. Cangiani, R. Davidchack, E. Georgoulis, A. Gorban, J. Levesley and M. Tretyakov eds.*, Springer, 2013; 851–859.
29. Perotto S, Veneziani A. Coupled model and grid adaptivity in hierarchical reduction of elliptic problems. *J. Sci. Comput.* 2014; **60**:505–536.
30. Perotto S, Zilio A. Space-time adaptive hierarchical model reduction for parabolic equations. *Adv. Model. and Simul. in Eng. Sci.* 2015; **2**:25.
31. Guzzetti S. *Hierarchical Model Reduction for Incompressible Flows in Cylindrical Domains* 2014. M.Sc. Thesis. Politecnico di Milano.
32. Blanco P, Mansilla Alvarez L, Feijóo R. Hybrid element-based approximation for the navierstokes equations in pipe-like domains. *Comp. Meth. Appl. Mech. Engrg.* 2015; **283**:971–993.
33. Aletti M, Perotto S, Veneziani A. Educated bases for the HiMod reduction of advection-diffusion-reaction problems with general boundary conditions. *Technical Report MOX 37/2015* 2015. URL www.mox.polimi.it.
34. Antiga L, Piccinelli M, Botti L, Ene-Iordache B, Remuzzi A, Steinman DA. An image-based modeling framework for patient-specific computational hemodynamics. *Medical & Biological Engineering & Computing* Nov 2008; **46**(11):1097–1112, doi:10.1007/s11517-008-0420-1.
35. Lorensen WE, Cline HE. Marching cubes: A high resolution 3d surface construction algorithm. *Computer Graphics* 1987; **21**(4):163–169.
36. Antiga L, Ene-Iordache B, Remuzzi A. Computational geometry for patient-specific reconstruction and meshing of blood vessels from MR and CT angiography. *IEEE Transactions on Medical Imaging* May 2003; **22**(5), doi: 10.1109/TMI.2003.812261.
37. VMTK. *Vascular Modeling Toolkit* 2015. Url: http://www.vmtk.org.
38. Jang I. *Cardiovascular OCT Imaging*. Springer International Publishing, Switzerland, 2015.
39. Yang B, Piccinelli M, Esposito G, Gogas B, Giddens D, Samady H, Veneziani A. Patient-specific cfd-oriented reconstruction of coronary arteries with BVS stents from OCT/Angiographies. *In Preparation* 2015; .
40. Arnold D, Brezzi F, Fortin M. A stable finite element for the Stokes equations. *Calcolo* 1984; (21).
41. Perotto S, Reali A, Rusconi P, Veneziani A. Higamod: A hierarchical isogeometric approach for model reduction in curved pipes. *Technical Report TR-2015-13* 2015. URL www.mathcs.emory.edu.